Time-Optimal Model Predictive Control of Permanent Magnet Synchronous Motors Considering Current and Torque Constraints

Anian Brosch ⬦, Oliver Wallscheid ⬦, *Member, IEEE*, and Joachim Böcker ⬦, *Senior Member, IEEE*

Abstract—In various permanent magnet synchronous motor (PMSM) drive applications the torque dynamics are an important performance criterion. Here, time-optimal control (TOC) methods can be utilized to achieve highest control dynamics. Applying the state-of-the-art TOC methods leads to unintended overcurrents and torque over- and undershoots during transient operation. To prevent these unintended control characteristics while still achieving TOC performance the time-optimal model predictive control (TO-MPC) is proposed in this work. The TO-MPC contains a reference prerotation (RPR) and a continuous control set model predictive flux control (CCS-MPFC). By applying Pontryagin's maximum principle, the TOC solution trajectories for states and inputs of the PMSM are determined neglecting current and torque limits. With the TOC solution, a flux linkage reference for the CCS-MPFC is calculated that corresponds to a prerotation of the operating point in the stator-fixed coordinate system. This prerotated flux linkage reference is reached in minimum time without overcurrents and torque over- as well as undershoots by incorporating current and torque limits as time-varying softened state constraints into the CCS-MPFC. Simulative and experimental investigations for linearly and non-LM-PMSMs in the whole speed and torque range show that, compared to state-of-the-art TOC methods, overcurrents and torque over- as well as undershoots are prevented by the proposed TO-MPC.

Index Terms—Continuous control set, model predictive control, permanent magnet synchronous motor (PMSM), time optimal control (TOC), torque control.

I. INTRODUCTION

DUE to the high torque and power densities of permanent magnet synchronous motors (PMSMs) with resulting low rotor inertia, PMSMs are well suited for highly dynamic applications. Since the torque control directly affects the jerk and acceleration of the drive, the torque response is an important performance criterion for characterizing the dynamics of the drive. Therefore, improving the torque response dynamics is an ongoing and important research topic in academia and industry [1], [2], [3], [4], [5], [6].

A. State-of-the-art Techniques

A desired torque can be achieved by various combinations of stator currents. Here, the operating point with the least losses is preferred. This loss-optimal reference operating point is usually calculated by an open-loop operating point controller (OPC) and fed to the underlying closed-loop controller. As control variables, currents or flux linkages in the stator- or rotor-fixed coordinate system can be used as well as the tupel consisting of torque and flux linkage amplitude.

To achieve time-optimal control (TOC) performance, the future transient state and input trajectories must be considered for optimization. Consequently, all controller types that do not optimize the whole future trajectory during transients, e.g., conventional proportional–integral field oriented control (PI-FOC) [7], deadbeat direct torque and flux control [8], and direct torque control [9] achieve time-suboptimal control performance. Particulary during larger torque variations, it may take many sampling periods to reach a new reference operating point. Accordingly, model predictive controllers (MPCs) [10], [11], [12], [13] may only achieve suboptimal control performance during transients because their prediction horizon is always restricted by computational capacity of the embedded controller device.

To increase the control dynamics to its maximum extent, control methods that solve the TOC problem online [2], [3], [4], [5], [6], must be applied. With the help of optimal control theory methods, e.g., Pontryagin's maximum principle, the TOC solution for input and state trajectories during transients for PMSMs can be derived. The resulting state trajectories reach the operating point in the shortest possible time. From previous publications in the field, two characteristics for the stator voltages $\boldsymbol{u}_{\alpha\beta} = [u_\alpha \quad u_\beta]^\intercal$ (input trajectories) in the stator-fixed $\alpha\beta$-coordinate system of the TOC solution during transients can be observed [2], [3] as follows.

1) The stator voltages $\boldsymbol{u}_{\alpha\beta}(t)$ are constant.
2) The stator voltages $\boldsymbol{u}_{\alpha\beta}(t)$ are saturated by the input constraint (voltage hexagon or a circular approximation of the voltage hexagon).

Constant $\boldsymbol{u}_{\alpha\beta}(t)$ voltages lead to a linearly shaped trajectory of the PMSM's flux linkage $\boldsymbol{\psi}_{\alpha\beta}(t)$ by neglecting the ohmic voltage drop, since the ordinary differential equation (ODE) of $\boldsymbol{\psi}_{\alpha\beta}(t)$ (Faraday's law of induction) is equal to an integrator, and the intersection of the input constraints ensures fastest possible movements of $\boldsymbol{\psi}_{\alpha\beta}(t)$ in the $\alpha\beta$ flux linkage plane. To
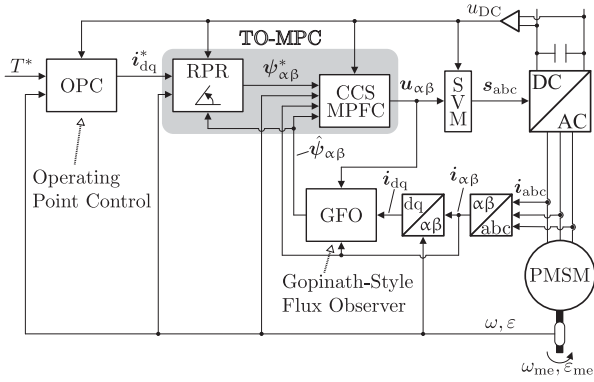
Fig. 1.   Overall control scheme (gray-shaded part is the focus of this article).

calculate this time-optimal stator voltage $\boldsymbol{u}_{\alpha\beta}$ during transients, a nonlinear equation system must be solved iteratively in an online fashion. The publications [2], [3], [4] solve the TOC problem in every sampling instant. Here, the bisection method as numerical solver with a constant number of iterations per sampling instant can be applied [3]. For the rotating reference chase control (RRCC) method proposed in [6], one iteration to solve the TOC problem per sampling instant is executed based on the TOC solution of the previous sampling instant. Compared to the methods [2], [3], [4], [5], only the RRCC takes transient overcurrents as well as torque over- and undershoots into account and tries to prevent them heuristically. Nevertheless, these transient overcurrents as well as torque over- and undershoots can be reduced compared to the TOC methods [2], [3], [4], [5], but not prevented with the RRCC, which is shown in Section VI.

B. Contribution

To prevent transient overcurrents as well as torque over- and undershoots in a TOC framework, the method of time-optimal model predictive control (TO-MPC)[1] is proposed in this article. The TO-MPC contains a continuous control set model predictive flux control (CCS-MPFC) and a reference pre-rotation (RPR) that manipulates the flux linkage reference of the CCS-MPFC and ensures TOC behavior, see Fig. 1. Reason for the application of the CCS-MPFC is that compared to other control methods, e.g., PI-FOC, an MPC provides the possibility to naturally take into account current and torque limits that can be formulated as time-varying softened state constraints.

Moreover, the propsed TO-MPC is incorporated in a torque control scheme, cf., Fig. 1, with the following additional elements.
1) OPC that selects loss-optimal reference currents $\boldsymbol{i}_{\mathrm{dq}}^*$ in the linear modulation range based on the maximum-torque-per-current (MTPC) and maximum-torque-per-voltage (MTPV) strategies [7], [14], [15].
2) Flux observer that estimates the PMSM's flux $\hat{\boldsymbol{\psi}}_{\alpha\beta}$ in the entire speed range including standstill [16], [17].

---

[1]Although the TOC methods proposed in [2], [3], [5], [6] require a model during online operation similar to the proposed approach, the name of the proposed control method is extended to TO-MPC since it contains an MPC characteristic formulation of the cost function and input, as well as state constraints.

3) Space vector modulation (SVM) scheme that converts the voltages $\boldsymbol{u}_{\alpha\beta}$ commanded by the CCS-MPFC into switching commands $\boldsymbol{s}_{\mathrm{abc}}$ [18].

The proposed RPR solves the set of nonlinear equations of TOC numerically in every sampling instant without considering torque and current limits. With the TOC solution, the reference flux linkage $\boldsymbol{\psi}_{\alpha\beta}^*$ for the CCS-MPFC is calculated. This flux linkage reference corresponds to a prerotation of the flux linkage reference $\boldsymbol{\psi}_{\mathrm{dq}}(\boldsymbol{i}_{\mathrm{dq}}^*)$ in the dq-coordinate system transformed to the $\alpha\beta$-coordinate system with the momentary electrical rotor angle ε. To steer the PMSM's flux linkage to the flux linkage reference of the RPR, the CCS-MPFC including torque and current limits is applied. As a result of the proposed TO-MPC, the following advantageous properties for the overall control scheme can be accomplished.
1) The TO-MPC is able to achieve minimum settling times during transient operation in the entire speed and torque range thanks to the reference flux linkage manipulation for the CCS-MPFC by the RPR.
2) Compared to TOC methods proposed in [2], [3], [4], [5], [6], overcurrents as well as torque over- and undershoots during transient operation are prevented by time-varying torque and current limits implemented as linear state constraints for the quadratic program (QP) of the CCS-MPFC.

C. Article Structure

The rest of this article is organized as follows. Section II describes the general control framework. The discrete-time prediction models for flux linkage, current, and torque are derived in Section III. In Section IV the RPR is presented. Section V focuses in detail on the CCS-MPFC. Extensive simulative and experimental investigations are discussed in Sections VI and VII. Finally, Section VIII concludes this article.

II. GENERAL CONTROL FRAMEWORK

In the following, the overall control scheme shown in Fig. 1 is explained in more detail.

A. Coordinate Systems

Transformations between the stator-fixed three-phase abc and the stator-fixed $\alpha\beta$-coordinate system are calculated with the following matrices:

$$\boldsymbol{T}_{\alpha\beta\mathrm{abc}} = \frac{2}{3}\begin{bmatrix} 1 & -\frac{1}{2} & -\frac{1}{2} \\ 0 & \frac{\sqrt{3}}{2} & -\frac{\sqrt{3}}{2} \end{bmatrix}, \quad \boldsymbol{T}_{\mathrm{abc}\alpha\beta} = \boldsymbol{T}_{\alpha\beta\mathrm{abc}}^{\dagger} \quad (1)$$

where, $\dagger$ denotes the Moore–Penrose pseudoinverse and bold symbols depict matrices/vectors. In a similar way, the transformations between the $\alpha\beta$ and rotor-fixed dq-coordinate system can be formulated as

$$\boldsymbol{T}_{\mathrm{dq}\alpha\beta}(\varepsilon(t)) = \begin{bmatrix} \cos(\varepsilon(t)) & \sin(\varepsilon(t)) \\ -\sin(\varepsilon(t)) & \cos(\varepsilon(t)) \end{bmatrix}$$

$$\boldsymbol{T}_{\alpha\beta\mathrm{dq}}(\varepsilon(t)) = \boldsymbol{T}_{\mathrm{dq}\alpha\beta}^{-1}(\varepsilon(t)) = \boldsymbol{T}_{\mathrm{dq}\alpha\beta}^{\mathsf{T}}(\varepsilon(t)). \quad (2)$$

With (1) and (2) the transformation between the abc- and dq-coordinate system evaluates to

$$\boldsymbol{T}_{\mathrm{dqabc}}(\varepsilon(t)) = \boldsymbol{T}_{\mathrm{dq\alpha\beta}}(\varepsilon(t))\boldsymbol{T}_{\alpha\beta\mathrm{abc}}$$

$$\boldsymbol{T}_{\mathrm{abcdq}}(\varepsilon(t)) = \boldsymbol{T}_{\mathrm{dqabc}}^{\dagger}(\varepsilon(t)). \tag{3}$$

B. Inverter

For a three-phase, two-level inverter, the stator voltages of a motor with star-connected windings are given by

$$\boldsymbol{u}_{\alpha\beta} \in \mathbb{U}_{\alpha\beta} = \left\{ \boldsymbol{u}_{\alpha\beta} \in \mathbb{R}^2 \,|\, \boldsymbol{u}_{\alpha\beta} = u_{\mathrm{DC}}\boldsymbol{T}_{\alpha\beta\mathrm{abc}}\boldsymbol{d}_{\mathrm{abc}} \right\} \tag{4}$$

where, u_{DC} is the dc-link voltage and $\boldsymbol{d}_{\mathrm{abc}} \in [0,1]^3$ the duty cycle vector of the inverter.

C. Operating Point Control

To minimize ohmic losses the operating point control (higher level open-loop torque controller) proposed in [14] is utilized, which selects the operating point $\boldsymbol{i}_{\mathrm{dq}}^*$ based on the MTPC and MTPV strategies. Here, the nonlinear magnetization with significant (cross-)saturation effects of highly utilized PMSMs are linearized online and optimal operating points $\boldsymbol{i}_{\mathrm{dq}}^*$ are calculated analytically. The nonlinear magnetization is taken into account iteratively with a successive linearization and analytical calculation of the subsequent optimal operating point. To reduce computation time only one iteration to calculate the optimal operating point per controller cycle (sampling instant) is executed by the OPC in this article.

D. Gopinath-Style Flux Observer

The CCS-MPFC requires the knowledge of the PMSM's momentary flux linkage $\boldsymbol{\psi}_{\alpha\beta}[k]$. Hence, the flux linkage is estimated with the help of a Gopinath-style flux observer [16], [17]. Here, the flux linkage estimate of a current model via a current-to-flux linkage look-up table (LUT), see Fig. 10, is combined with the flux linkage estimate of a voltage model (6).

III. DISCRETE-TIME PMSM MODEL

The proposed TO-MPC requires motor model variants for predicting the flux linkage in the $\alpha\beta$-coordinate system, the current in the dq-coordinate system [19], [20], [21], as well as the airgap torque. These models are derived in the following.

A. Flux Linkage Model in the $\alpha\beta$-Coordinate System

According to Faraday's law of induction, the differential equation of the flux linkages $\boldsymbol{\psi}_{\alpha\beta} = [\psi_\alpha \quad \psi_\beta]^\intercal$ for a PMSM can be described as follows:

$$\frac{\mathrm{d}}{\mathrm{d}t}\boldsymbol{\psi}_{\alpha\beta}(t) = \boldsymbol{u}_{\alpha\beta}(t) - R_{\mathrm{s}}\boldsymbol{i}_{\alpha\beta}(t) \tag{5}$$

where, $\boldsymbol{i}_{\alpha\beta} = [i_\alpha \quad i_\beta]^\intercal$ represents the stator current, and R_{s} the ohmic stator resistance. By applying the forward Euler method with a sampling time T_{s}, the discrete-time flux linkage difference equation in the $\alpha\beta$-coordinate system is given by

$$\boldsymbol{\psi}_{\alpha\beta}[k+1] = \boldsymbol{A}_{\boldsymbol{\psi}}\boldsymbol{\psi}_{\alpha\beta}[k] + \boldsymbol{B}_{\boldsymbol{\psi}}\boldsymbol{u}_{\alpha\beta}[k] + \boldsymbol{E}_{\boldsymbol{\psi}}[k]$$

with:

$$\boldsymbol{A}_{\boldsymbol{\psi}} = \boldsymbol{I}$$

$$\boldsymbol{B}_{\boldsymbol{\psi}} = T_{\mathrm{s}}\boldsymbol{I}$$

$$\boldsymbol{E}_{\boldsymbol{\psi}}[k] = -T_{\mathrm{s}}R_{\mathrm{s}}\boldsymbol{i}_{\alpha\beta}[k] \tag{6}$$

where, $\boldsymbol{I}$ is the identity matrix.

B. Current Model in the dq-Coordinate System

To derive the difference equation of the current $\boldsymbol{i}_{\mathrm{dq}}$, the motor model (6) must be transformed to the dq-coordinate system

$$\boldsymbol{\psi}_{\mathrm{dq}}[k+1]$$
$$= \boldsymbol{T}_{\alpha\beta\mathrm{dq}}(-T_{\mathrm{s}}\omega[k])(\boldsymbol{\psi}_{\mathrm{dq}}[k] + T_{\mathrm{s}}(\boldsymbol{u}_{\mathrm{dq}}[k] - R_{\mathrm{s}}\boldsymbol{i}_{\mathrm{dq}}[k])) \tag{7}$$

with the identity

$$\boldsymbol{T}_{\alpha\beta\mathrm{dq}}(\varepsilon[k] - \varepsilon[k+1]) = \boldsymbol{T}_{\mathrm{dq\alpha\beta}}(\varepsilon[k+1])\boldsymbol{T}_{\alpha\beta\mathrm{dq}}(\varepsilon[k]) \tag{8}$$

and the approximation $T_{\mathrm{s}}\omega[k] \approx \varepsilon[k+1] - \varepsilon[k]$. The term $\boldsymbol{T}_{\alpha\beta\mathrm{dq}}(-T_{\mathrm{s}}\omega[k])$ considers the rotation of the dq against the $\alpha\beta$-coordinate system during one sampling period with the electrical angular velocity ω [19], [20], [21]. To link the variation in flux linkage $\boldsymbol{\psi}_{\mathrm{dq}}$ with the variation in current $\boldsymbol{i}_{\mathrm{dq}}$, the differential inductance matrix

$$\boldsymbol{L}_{\mathrm{dq},\Delta}(\boldsymbol{i}_{\mathrm{dq}}) = \begin{bmatrix} L_{\mathrm{dd}}(\boldsymbol{i}_{\mathrm{dq}}) & L_{\mathrm{dq}}(\boldsymbol{i}_{\mathrm{dq}}) \\ L_{\mathrm{qd}}(\boldsymbol{i}_{\mathrm{dq}}) & L_{\mathrm{qq}}(\boldsymbol{i}_{\mathrm{dq}}) \end{bmatrix} = \begin{bmatrix} \frac{\partial\psi_{\mathrm{d}}}{\partial i_{\mathrm{d}}} & \frac{\partial\psi_{\mathrm{d}}}{\partial i_{\mathrm{q}}} \\ \frac{\partial\psi_{\mathrm{q}}}{\partial i_{\mathrm{d}}} & \frac{\partial\psi_{\mathrm{q}}}{\partial i_{\mathrm{q}}} \end{bmatrix} \tag{9}$$

must be applied. By approximating (9)

$$\underbrace{\Delta\boldsymbol{\psi}_{\mathrm{dq}}[k+1]}_{\boldsymbol{\psi}_{\mathrm{dq}}[k+1] - \boldsymbol{\psi}_{\mathrm{dq}}[k]} \approx \boldsymbol{L}_{\mathrm{dq},\Delta}(\boldsymbol{i}_{\mathrm{dq}}[k]) \underbrace{\Delta\boldsymbol{i}_{\mathrm{dq}}[k+1]}_{\boldsymbol{i}_{\mathrm{dq}}[k+1] - \boldsymbol{i}_{\mathrm{dq}}[k]} \tag{10}$$

and inserting (10) in (7), the discrete-time current difference equation of a PMSM considering (cross-)saturation effects in the dq-coordinate system evaluates to

$$\boldsymbol{i}_{\mathrm{dq}}[k+1] = \boldsymbol{A}_{\boldsymbol{i}}(\boldsymbol{i}_{\mathrm{dq}}[k])\boldsymbol{i}_{\mathrm{dq}}[k] + \boldsymbol{B}_{\boldsymbol{i}}(\boldsymbol{i}_{\mathrm{dq}}[k],\omega[k])\boldsymbol{u}_{\mathrm{dq}}[k]$$
$$+ \boldsymbol{E}_{\boldsymbol{i}}(\boldsymbol{i}_{\mathrm{dq}}[k],\omega[k])$$

with:

$$\boldsymbol{A}_{\boldsymbol{i}}(\boldsymbol{i}_{\mathrm{dq}}[k]) = \boldsymbol{I} - \boldsymbol{L}_{\mathrm{dq},\Delta}^{-1}(\boldsymbol{i}_{\mathrm{dq}}[k])R_{\mathrm{s}}T_{\mathrm{s}}$$

$$\boldsymbol{B}_{\boldsymbol{i}}(\boldsymbol{i}_{\mathrm{dq}}[k],\omega[k]) = \boldsymbol{L}_{\mathrm{dq},\Delta}^{-1}(\boldsymbol{i}_{\mathrm{dq}}[k])\boldsymbol{T}_{\alpha\beta\mathrm{dq}}(-T_{\mathrm{s}}\omega[k])T_{\mathrm{s}}$$

$$\boldsymbol{E}_{\boldsymbol{i}}(\boldsymbol{i}_{\mathrm{dq}}[k],\omega[k]) = \boldsymbol{L}_{\mathrm{dq},\Delta}^{-1}(\boldsymbol{i}_{\mathrm{dq}}[k])$$
$$[\boldsymbol{T}_{\alpha\beta\mathrm{dq}}(-T_{\mathrm{s}}\omega[k]) - \boldsymbol{I}]\,\boldsymbol{\psi}_{\mathrm{dq}}(\boldsymbol{i}_{\mathrm{dq}}[k]). \tag{11}$$

C. Torque Model

The airgap torque of the PMSM is given by

$$T[k] = \frac{3}{2}p\left(\psi_{\mathrm{d}}[k]i_{\mathrm{q}}[k] - \psi_{\mathrm{q}}[k]i_{\mathrm{d}}[k]\right). \tag{12}$$

By linearizing (12) with respect to the current, the torque-to-current relation can be approximated by

$$T[k+1] = T[k] + \frac{\partial T}{\partial \boldsymbol{i}_{\mathrm{dq}}} \underbrace{(\boldsymbol{i}_{\mathrm{dq}}[k+1] - \boldsymbol{i}_{\mathrm{dq}}[k])}_{\Delta \boldsymbol{i}_{\mathrm{dq}}[k+1]}. \tag{13}$$

Here, the partial derivative

$$\frac{\partial T}{\partial \boldsymbol{i}_{\mathrm{dq}}} = \frac{3}{2}p \begin{bmatrix} L_{\mathrm{dd}}[k]i_{\mathrm{q}}[k] - L_{\mathrm{qd}}[k]i_{\mathrm{d}}[k] - \psi_{\mathrm{q}}[k] \\ L_{\mathrm{dq}}[k]i_{\mathrm{q}}[k] - L_{\mathrm{qq}}[k]i_{\mathrm{d}}[k] + \psi_{\mathrm{d}}[k] \end{bmatrix}^{\mathsf{T}} \tag{14}$$

is calculated from (12) and (9). The current difference $\Delta \boldsymbol{i}_{\mathrm{dq}}$ in (13) can be expressed as

$$\Delta \boldsymbol{i}_{\mathrm{dq}}[k+1] = (\boldsymbol{A_i}[k] - \boldsymbol{I}) \, \boldsymbol{i}_{\mathrm{dq}}[k] + \boldsymbol{B_i}[k]\boldsymbol{u}_{\mathrm{dq}}[k] + \boldsymbol{E_i}[k] \tag{15}$$

using the current model (11). Inserting (15) in (13) leads to the following torque model:

$$T[k+1] = \boldsymbol{A}_T T[k] + \boldsymbol{B}_T[k]\boldsymbol{u}_{\mathrm{dq}}[k] + \boldsymbol{E}_T[k]$$

with:

$$\boldsymbol{A}_T = \boldsymbol{I}$$

$$\boldsymbol{B}_T[k] = \frac{\partial T}{\partial \boldsymbol{i}_{\mathrm{dq}}} \boldsymbol{B_i}[k]$$

$$\boldsymbol{E}_T[k] = \frac{\partial T}{\partial \boldsymbol{i}_{\mathrm{dq}}} ((\boldsymbol{A_i}[k] - \boldsymbol{I}) \, \boldsymbol{i}_{\mathrm{dq}}[k] + \boldsymbol{E_i}[k]) . \tag{16}$$

IV. REFERENCE PREROTATION

The task of the RPR is to calculate a reference flux linkage $\boldsymbol{\psi}_{\alpha\beta}^*[k+1]$ without respect to overcurrents as well as torque over- and undershoots for the CCS-MPFC such that the required time to reach the operating point $\boldsymbol{i}_{\mathrm{dq}}^*$ during transient operation is minimal. The RPR, therefore, inherently solves the TOC problem.

A. Steady-State Control Conditions

During steady-state control conditions $\boldsymbol{i}_{\mathrm{dq}}^*[k] = \boldsymbol{i}_{\mathrm{dq}}[k]$, the reference flux linkage must be equal to

$$\boldsymbol{\psi}_{\alpha\beta}^*[k+1] = \boldsymbol{T}_{\alpha\beta\mathrm{dq}} \left(\omega[k]T_{\mathrm{s}}\right) \underbrace{\boldsymbol{T}_{\alpha\beta\mathrm{dq}} \left(\varepsilon[k]\right) \boldsymbol{\psi}_{\mathrm{dq}} \left(\boldsymbol{i}_{\mathrm{dq}}^*[k]\right)}_{\boldsymbol{\psi}_{\alpha\beta}\left(\boldsymbol{i}_{\mathrm{dq}}^*, \varepsilon\right)}. \tag{17}$$

The flux linkage reference $\boldsymbol{\psi}_{\mathrm{dq}}(\boldsymbol{i}_{\mathrm{dq}}^*[k])$ in (17) is derived with a current-to-flux linkage LUT, see Fig. 10, for the operating point $\boldsymbol{i}_{\mathrm{dq}}^*$, which is calculated by the OPC, to take (cross-)saturation effects into account. For a constant operating point $\boldsymbol{i}_{\mathrm{dq}}^*$ and speed ω, in the linear modulation range, the operating point in the $\alpha\beta$ flux linkage coordinate system $\boldsymbol{\psi}_{\alpha\beta}(\boldsymbol{i}_{\mathrm{dq}}^*, \varepsilon)$ rotates with a constant magnitude and angular velocity ω, cf., (17) and Fig. 3(b).

B. Transient Control Conditions

During transient control conditions the RPR must solve the TOC problem. For a general nonlinear dynamical system the

TOC problem is given by

$$\min_{\boldsymbol{u}(t)} \tilde{t} \tag{18a}$$

$$\text{s.t.} \quad \frac{\mathrm{d}}{\mathrm{d}t}\boldsymbol{x}(t) = \boldsymbol{f}(\boldsymbol{x}(t), \boldsymbol{u}(t), t) \tag{18b}$$

$$\boldsymbol{x}(0) = \boldsymbol{x}_0 \tag{18c}$$

$$\boldsymbol{x}(\tilde{t}) = \boldsymbol{x}^* \tag{18d}$$

$$\boldsymbol{x}(t) \in \mathbb{X} \tag{18e}$$

$$\boldsymbol{u}(t) \in \mathbb{U} \tag{18f}$$

where, the time $\tilde{t}$ (18a) is minimized that is needed to steer a dynamical system (18b) from an initial state $\boldsymbol{x}_0$ (18c) to its reference $\boldsymbol{x}^*$ (18d) with respect to state (18e) and input constraints (18f). In this work the differential equation characterizing the dynamical system (18b) corresponds to Faraday's law of induction (5), the state $\boldsymbol{x}$ corresponds du the flux linkage $\boldsymbol{\psi}_{\alpha\beta}$, the input $\boldsymbol{u}$ to the voltages $\boldsymbol{u}_{\alpha\beta}$, the state constraints to current and torque constraints, and the input constraints to the voltage hexagon.

By applying Pontryagin's maximum principle to find the time-optimal stator voltages $\boldsymbol{u}_{\alpha\beta}(t)$, i.e., solving the TOC problem, during transients to steer the PMSM's flux $\boldsymbol{\psi}_{\alpha\beta}$ to its reference $\boldsymbol{\psi}_{\alpha\beta}^*$ for neglected state constraints, e.g., overcurrents and torque over- and undershoots, the following two characteristics are valid [2], [3].

1) The stator voltages $\boldsymbol{u}_{\alpha\beta}(t)$ are constant.
2) The stator voltages $\boldsymbol{u}_{\alpha\beta}(t)$ are saturated by the input constraint.

This results in linearly shaped trajectories of the flux linkage $\boldsymbol{\psi}_{\alpha\beta}(t)$ of the PMSM when neglecting the ohmic voltage drop.

To calculate this time-optimal stator voltage, a set of nonlinear equations for the time $\tilde{t}$, that is needed to steer the PMSM's flux $\boldsymbol{\psi}_{\alpha\beta}$ to its reference $\boldsymbol{\psi}_{\alpha\beta}^*$, and the stator voltage $\boldsymbol{u}_{\alpha\beta}$ must be solved [2], [3]

$$\underbrace{\boldsymbol{T}_{\alpha\beta\mathrm{dq}} \left(\varepsilon[k] + \omega[k]\tilde{t}\right) \boldsymbol{\psi}_{\mathrm{dq}} \left(\boldsymbol{i}_{\mathrm{dq}}^*[k]\right)}_{\boldsymbol{\psi}_{\alpha\beta}^*\left(kT_{\mathrm{s}} + \tilde{t}\right)} = \underbrace{\boldsymbol{\psi}_{\alpha\beta}[k] + \tilde{t}\boldsymbol{u}_{\alpha\beta}}_{\boldsymbol{\psi}_{\alpha\beta}\left(kT_{\mathrm{s}} + \tilde{t}, \boldsymbol{u}_{\alpha\beta}\right)} \tag{19a}$$

$$\|\boldsymbol{u}_{\alpha\beta}\| = u_{\max} \tag{19b}$$

where, the voltage drop of the ohmic stator resistance R_{s} is neglected and $u_{\max}$ represents a circular approximation of the voltage hexagon. This approximation is set to

$$u_{\max} = \frac{2}{\pi} u_{\mathrm{DC}}[k] \tag{20}$$

which corresponds to the fundamental voltage of six-step operation [22]. The left-hand side of (19a) represents the prerotation of the flux reference $\boldsymbol{\psi}_{\alpha\beta}^*$ as a function of the rotation angle $\omega[k]\tilde{t}$ and the right-hand side represents the linear evolution of $\boldsymbol{\psi}_{\alpha\beta}$ as a function of $\tilde{t}$ and $\boldsymbol{u}_{\alpha\beta}$. After a time duration of $\tilde{t}$, the predicted flux $\boldsymbol{\psi}_{\alpha\beta}$ must coincide with the reference flux $\boldsymbol{\psi}_{\alpha\beta}^*$, whereby a constant voltage $\boldsymbol{u}_{\alpha\beta}$ with maximum amplitude $u_{\max}$ is applied.

To solve the system of nonlinear equations (19) in every sampling instant, numerical methods must be applied. A method
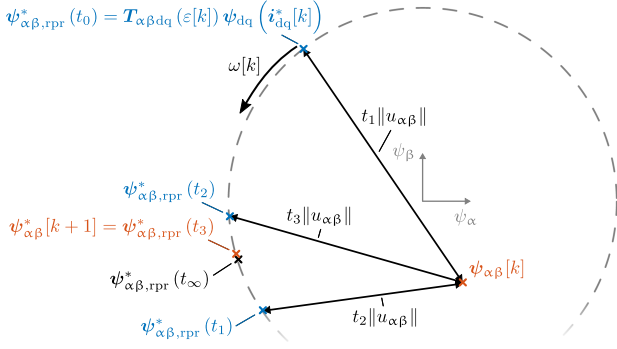
Fig. 2. Illustration of the RPR procedure with $N = 3$.

to iteratively solve (19) for $\tilde{t}$ is given in pseudocode Algorithm 1 from line 1 to 9 and a graphical representation is depicted in Fig. 2. Here, N iteration steps are performed from line 6 to 9 to approximate the solution of (19) with $\tilde{t} \approx \tilde{t}_N$ and $\psi^*_{\alpha\beta}(kT_s + \tilde{t}) \approx \psi^*_{\alpha\beta,N}$. The iteration step from line 6 to 9 is similar to the iteration step that is only performed once per sampling instant, which is proposed for the RRCC in [4]. In line 10–14 of Algorithm 1, a distinction between transient and steady-state control operation is made. If the time $\tilde{t}$ to steer $\psi_{\alpha\beta}$ to its reference $\psi^*_{\alpha\beta}$ is smaller than a chosen threshold t_{thresh}, steady-state control operation is present and $\psi^*_{\alpha\beta}[k+1]$ is set according to (17). Otherwise, the controller is in a transient operation state and the reference $\psi^*_{\alpha\beta}$ is prerotated by the angle $\omega\tilde{t}$, cf., (19a). The threshold t_{thresh} is a tuning parameter and must be set to $t_{\text{thresh}} \geq T_s$. Here, $t_{\text{thresh}} = T_s$ would be the obvious choice. Since the voltage hexagon is approximated circularly, slightly increased values for t_{thresh} are recommended, e.g., $t_{\text{thresh}} = 1.1T_s \dots 1.5T_s$.

Applying the deadbeat flux control law

$$\boldsymbol{u}_{\alpha\beta}[k] = \frac{\boldsymbol{\psi}^*_{\alpha\beta}[k+1] - \boldsymbol{\psi}_{\alpha\beta}[k]}{T_s} + R_s \boldsymbol{i}_{\alpha\beta}[k] \qquad (21)$$

with the calculated flux linkage reference $\psi^*_{\alpha\beta}[k+1]$ of the RPR results in time-optimal transient and accurate steady-state operation. To saturate the voltages (21) to the voltage hexagon, the minimum phase error dynamic overmodulation scheme [23] must be applied.

However, TOC performance is achieved by applying the deadbeat flux control (21) with the RPR, neither unintended violations of the current limit nor over- and undershoots of the torque can be prevented. This is shown by a simulation, cf., Fig. 3, with steps in the reference torque T^* and the corresponding reference currents $\boldsymbol{i}^*_{\text{dq}}$ calculated by the OPC. For the sake of clarity, only the discrete-time samples with $T_s = 62.5\,\mu\text{s}$ that are synchronized with the SVM are shown. Therefore, the current, torque, and flux ripples induced by the switching of the inverter are not visible in the following figures. For this simulation a linearly magnetized PMSM (LM-PMSM), with the parameters given in Table I, is used.

In Fig. 3(a), the flux linkage reference $\psi^*_{\alpha\beta}$, calculated by the RPR, and the resulting $\boldsymbol{u}_{\alpha\beta}$, calculated with the deadbeat control law (21), are depicted. Here, nearly constant flux linkage
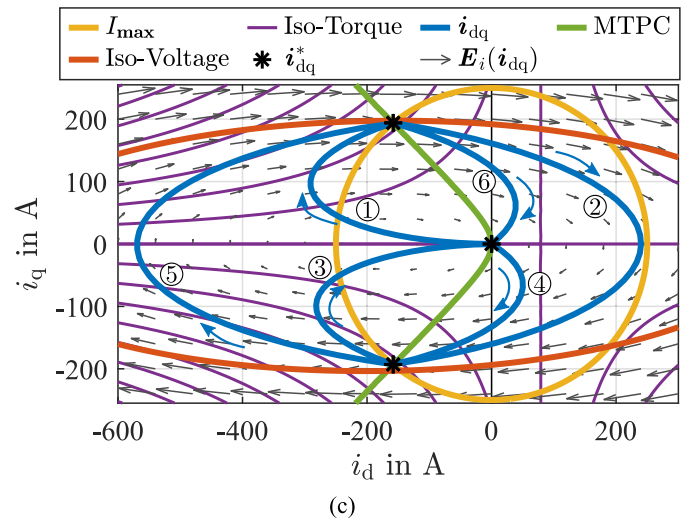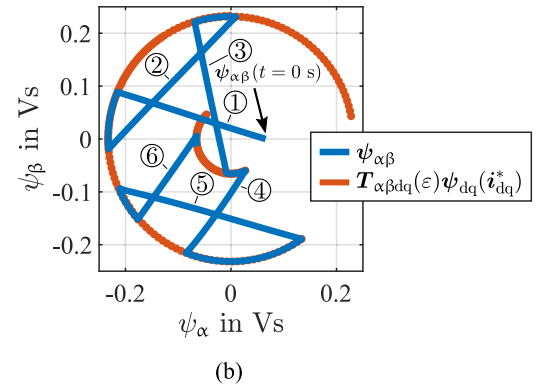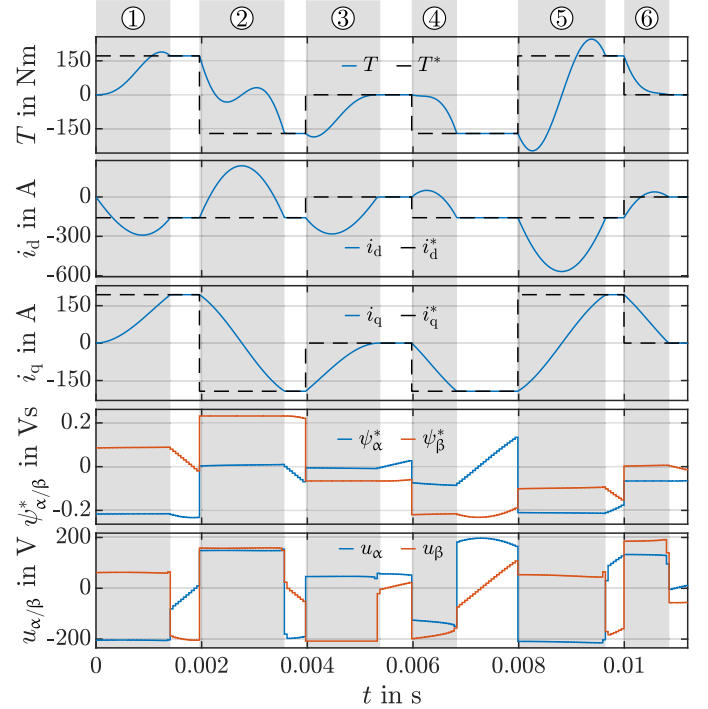

Fig. 3. Exemplary trajectories with the RPR ($t_{\text{thresh}} = 1.5T_s$, $N = 10$), the deadbeat flux control law (21), and the initial condition $\varepsilon(t = 0\,\text{s}) = 0$ at nominal speed ($n_{\text{me}} = 2750\,\text{min}^{-1}$). (a) Time courses. (b) Flux linkage trajectories. (c) Current trajectories.

TABLE I
LM-PMSM MODEL PARAMETERS

Nominal speed	n_{me}	$2750\,\mathrm{min}^{-1}$
Nominal torque	T_{nom}	$172\,\mathrm{Nm}$
Nominal current	I	$177\,\mathrm{A}$
Pole pair number	p	3
DC-link voltage	u_{DC}	$360\,\mathrm{V}$
Stator resistance	R_{s}	$18\,\mathrm{m\Omega}$
Permanent magnet flux	ψ_{p}	$68\,\mathrm{mVs}$
Inductances	L_{d}	$0.37\,\mathrm{mH}$
	L_{q}	$1.2\,\mathrm{mH}$

Algorithm 1: Reference Prerotation.

Input: $\boldsymbol{i}^*_{\mathrm{dq}}[k], u_{\mathrm{DC}}[k], \omega[k], \varepsilon[k], \boldsymbol{\psi}_{\alpha\beta}[k], T_{\mathrm{s}}$
Output: $\boldsymbol{\psi}^*_{\alpha\beta}[k+1]$
1: Choose $t_{\mathrm{thresh}} \in \mathbb{R}$ s.t. $t_{\mathrm{thresh}} \geq T_{\mathrm{s}}$
2: Choose $N \in \mathbb{N}$
3: Initialize $\tilde{t}_0 = 0\,\mathrm{s}$
4: Initialize $\psi^*_{\alpha\beta,0} = \boldsymbol{T}_{\alpha\beta\mathrm{dq}}(\varepsilon[k])\boldsymbol{\psi}_{\mathrm{dq}}(\boldsymbol{i}^*_{\mathrm{dq}}[k])$
5: Set $\|\boldsymbol{u}_{\alpha\beta}\| = \frac{2}{\pi}u_{\mathrm{DC}}[k]$
6: **for** $n = 1$ to N **do**
7:      $\tilde{t}_n = \frac{\|\psi^*_{\alpha\beta,n-1}-\boldsymbol{\psi}_{\alpha\beta}[k]\|}{\|\boldsymbol{u}_{\alpha\beta}\|}$
8:      $\psi^*_{\alpha\beta,n} = \boldsymbol{T}_{\alpha\beta\mathrm{dq}}(\omega[k]\tilde{t}_n)\psi^*_{\alpha\beta,0}$
9: **end for**
10: **if** $\tilde{t}_N > t_{\mathrm{thresh}}$ **then**
11:     $\boldsymbol{\psi}^*_{\alpha\beta}[k+1] = \psi^*_{\alpha\beta,N}$
12: **else**
13:     $\boldsymbol{\psi}^*_{\alpha\beta}[k+1] = \boldsymbol{T}_{\alpha\beta\mathrm{dq}}(\varepsilon[k]+\omega[k]T_{\mathrm{s}})\boldsymbol{\psi}_{\mathrm{dq}}(\boldsymbol{i}^*_{\mathrm{dq}}[k])$
14: **end if**

---

references $\boldsymbol{\psi}^*_{\alpha\beta}$ and voltages $\boldsymbol{u}_{\alpha\beta}$ during transients can be seen. The slight deviations of constant voltages $\boldsymbol{u}_{\alpha\beta}$ during transients are caused by RPR with the circular approximation of the voltage hexagon, the neglected ohmic voltage drop, and the finite number of iterations. However, these deviations can be considered as minor, which results in the characteristic time-optimal linear evolution of the flux linkage $\boldsymbol{\psi}_{\alpha\beta}$ during transients in the $\alpha\beta$ flux linkage plane, cf., Fig. 3(b).

Furthermore, the time-optimal trajectories can be visualized in the dq current coordinate system, see Fig. 3(c). Here, the current change caused by the induced voltage, characterized by $\boldsymbol{E}_i(\boldsymbol{i}_{\mathrm{dq}})$, is optimally exploited by the RPR to achieve TOC performance. Nevertheless, current limits are violated and over- and undershoots of the torque cannot be avoided, see Fig. 3(a) and (c).

To investigate the influence of the number of RPR iterations N on the control performance, the transients ① and ② of the scenario depicted in Fig. 3 are shown in Fig. 4 for $N = \{0; 1; 2; 5; 100\}$. For $N = 0$ no prerotation of the flux linkage reference is conducted and $N = 100$ represents an approximation of $N = \infty$. It can be seen that the deadbeat controller without prerotation of the reference ($N = 0$) is not able to reach its reference within the given time. For $N \geq 5$ the time-optimal characteristic linearly shaped flux linkage trajectories during transient operation are achieved due to the fast convergence of the RPR. Increasing N to more than 5 would not improve the
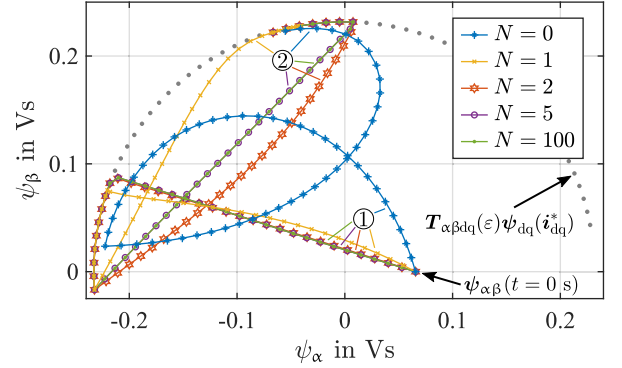

Fig. 4.   Flux linkage trajectories for the transients ① and ② of the scenario shown in Fig. 3 for $N = \{0; 1; 2; 5; 100\}$.
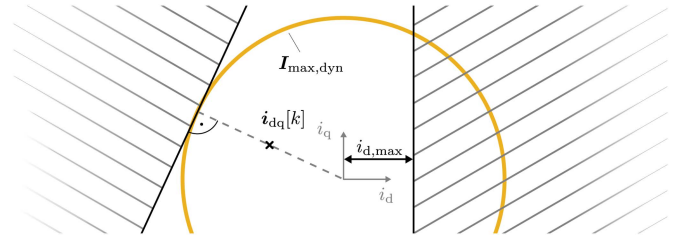

Fig. 5.   Linear time-varying current constraint approximation to prevent overcurrents as well as nonmonotonic torque dynamics induced by positive i_{d} currents.

results significantly but increase the computational load, which is not desirable.

V. CONTINUOUS CONTROL SET MODEL PREDICTIVE FLUX CONTROL

To overcome the unintended control characteristic of time-optimal controllers that do not consider current and torque limits during transient operation, e.g., [2], [3], [5] or the deadbeat controller (21), a CCS-MPFC with state and input constraints and the reference flux linkage $\boldsymbol{\psi}^*_{\alpha\beta}$ calculated by the RPR, is proposed in the following. With the help of state constraints for the CCS-MPFC, current limits are taken into account and over- as well as undershoots of the torque are prevented.

A. Current Constraints

Although the OPC selects operating points $\boldsymbol{i}^*_{\mathrm{dq}}$ within the current limit $I_{\max}$, this limit can be violated during transient processes, see Fig. 3(c). This can lead to thermal overload or increased thermal cycling of the inverter semiconductors due to their small thermal time constants. To prevent this, a dynamic current limit $I_{\max,\mathrm{dyn}}$ is introduced. The dynamic current limit is a tuning parameter and must satisfy $I_{\max,\mathrm{dyn}} \geq I_{\max}$.

Incorporating a circular current constraint for the predicted current $\boldsymbol{i}_{\mathrm{dq}}[k+1]$ into the CCS-MPFC would lead to an optimization problem with quadratic inequality constraints. Since these would increase the computational burden further than linear inequality constraints, the circular dynamic current constraint $I_{\max,\mathrm{dyn}}$ is approximated with a linear time-varying current constraint, see Fig. 5. This current constraint can be formulated as a linear inequality constraint for the predicted

current $i_{\mathrm{dq}}[k+1]$

$$\frac{(i_{\mathrm{dq}}[k])^\mathsf{T}}{\|i_{\mathrm{dq}}[k]\|} i_{\mathrm{dq}}[k+1] \leq I_{\mathrm{max,dyn}}. \tag{22}$$

To prevent nonmonotonic torque dynamics due to positive i_{d} currents, as it can be seen in the operating point change ② in Fig. 3(c), an additional linear current constraint

$$i_{\mathrm{d}}[k+1] \leq i_{\mathrm{d,max}} \tag{23}$$

with the tuning parameter $i_{\mathrm{d,max}} \geq 0$ A can be added, see Fig. 5. Both current constraints (22) and (23) can be rewritten in matrix-vector notation

$$\underbrace{\begin{bmatrix} 0 & 1 \\ i_{\mathrm{d}}[k] & i_{\mathrm{q}}[k] \end{bmatrix}}_{\mathcal{A}_{\mathcal{I}}[k]} i_{\mathrm{dq}}[k+1] \leq \underbrace{\begin{bmatrix} i_{\mathrm{d,max}} \\ I_{\mathrm{max,dyn}} \|i_{\mathrm{dq}}[k]\| \end{bmatrix}}_{b_{\mathcal{I}}[k]}. \tag{24}$$

To solve the optimization problem of the CCS-MPFC (32), the inequality constraint (24) for the predicted current $i_{\mathrm{dq}}[k+1]$ must be mapped to the input and optimization variable $u_{\alpha\beta}[k]$. This can be done by inserting the current prediction model (11) with the momentary current $i_{\mathrm{dq}}[k]$ in (24)

$$\mathcal{A}_{\mathcal{I}}[k] \underbrace{(A_i[k]i_{\mathrm{dq}}[k] + B_i[k]u_{\mathrm{dq}}[k] + E_i[k])}_{i_{\mathrm{dq}}[k+1]} \leq b_{\mathcal{I}}[k]$$

$$\Leftrightarrow \underbrace{\mathcal{A}_{\mathcal{I}}[k]B_i[k]T_{\mathrm{dq}\alpha\beta}\,(\varepsilon[k])}_{\mathcal{A}'_{\mathcal{I}}[k]} u_{\alpha\beta}[k]$$

$$\leq \underbrace{b_{\mathcal{I}}[k] - \mathcal{A}_{\mathcal{I}}[k]\,(A_i[k]i_{\mathrm{dq}}[k] + E_i[k])}_{b'_{\mathcal{I}}[k]}. \tag{25}$$

B. Torque Constraints

To prevent over- as well as undershoots and to ensure monotonic torque trajectories during transients, the predicted torque $T[k+1]$ must satisfy

$$T[k] \leq T[k+1] \leq T^* \text{ if } T[k] \leq T^* \tag{26}$$

or

$$T[k] \geq T[k+1] \geq T^* \text{ if } T[k] > T^*. \tag{27}$$

Both conditions (26) and (27) can be considered with

$$\mathrm{sign}\,(T^* - T[k])\,T[k+1] \leq \mathrm{sign}\,(T^* - T[k])\,T^* \tag{28}$$

and

$$\mathrm{sign}\,(T^* - T[k])\,T[k+1] \geq \mathrm{sign}\,(T^* - T[k])\,T[k]. \tag{29}$$

Furthermore, (28) and (29) can be rewritten in vector notation

$$\underbrace{\mathrm{sign}\,(T^* - T[k]) \begin{bmatrix} 1 \\ -1 \end{bmatrix}}_{\mathcal{A}_{\mathcal{T}}[k]} T[k+1] \leq \underbrace{\mathrm{sign}\,(T^* - T[k]) \begin{bmatrix} T^* \\ -T[k] \end{bmatrix}}_{b_{\mathcal{T}}[k]}. \tag{30}$$

Similarly to the current constraint (24), the torque constraint (30) must be mapped to the optimization variable $u_{\alpha\beta}[k]$ of the CCS-MPFC (32). This is achieved by inserting the torque

prediction model (16) with the momentary estimated torque $T[k]$ in (30)

$$\underbrace{\mathcal{A}_{\mathcal{T}}[k]B_T[k]T_{\mathrm{dq}\alpha\beta}\,(\varepsilon[k])}_{\mathcal{A}'_{\mathcal{T}}[k]} u_{\alpha\beta}[k]$$

$$\leq \underbrace{b_{\mathcal{T}}[k] - \mathcal{A}_{\mathcal{T}}[k]\,(A_T T[k] + E_T[k])}_{b'_{\mathcal{T}}[k]}. \tag{31}$$

C. Quadratic Optimization Problem

The cost function of the CCS-MPFC is designed to penalize the Euclidean distance from the predicted flux $\hat{\psi}_{\alpha\beta}[k+1]$ to the reference flux linkage $\psi^*_{\alpha\beta}[k+1]$ of the RPR, cf., Section IV. Furthermore, input constraints (voltage hexagon) and state constraints (torque and current, cf., Sections V-A and V-B) must be fulfilled. Thus, the optimization problem can be defined as

$$\min_{u_{\alpha\beta}[k]} \left\| \hat{\psi}_{\alpha\beta}[k+1] - \psi^*_{\alpha\beta}[k+1] \right\|^2 \tag{32a}$$

$$\text{s.t. } \hat{\psi}_{\alpha\beta}[k+1] = A_\psi \hat{\psi}_{\alpha\beta}[k] + B_\psi u_{\alpha\beta}[k] + E_\psi[k] \tag{32b}$$

$$\begin{bmatrix} \mathcal{A}'_{\mathcal{I}}[k] \\ \mathcal{A}'_{\mathcal{T}}[k] \end{bmatrix} u_{\alpha\beta}[k] \leq \begin{bmatrix} b'_{\mathcal{I}}[k] \\ b'_{\mathcal{T}}[k] \end{bmatrix} \tag{32c}$$

$$u_{\alpha\beta}[k] \in \mathbb{U}_{\alpha\beta}. \tag{32d}$$

For the practical implementation of this contribution the state constraints (32c) were softened with the help of a slack variable formulation to ensure feasibility of the optimization problem [24], [25]. To solve the linearly constrained quadratic program (32), any standard QP solver can be utilized. In this work, the embedded solver of the MATLAB MPC toolbox was chosen [26], [27]. To compensate for the control delay due to the digital implementation, a one-step state prediction is applied before the QP solver is called [28].

VI. SIMULATIVE INVESTIGATION

On the basis of a simulation, the TO-MPC (RPR combined with the CCS-MPFC of Section V) is investigated. The LM-PMSM motor model characterized by Table I is applied for this study. All following simulative investigations were conducted with the software Simulink from MathWorks. Here, the inverter and motor are modeled in a quasi-time continuous environment based on their equations reported in Sections II and III. The TO-MPC is simulated in a discrete-time subsystem with the controller sampling time $T_{\mathrm{s}} = 62.5\,\mu\mathrm{s}$. The resulting ODE of the Simulink model is solved with the adaptive Runge–Kutta method ode45 [29]. The parameters of the TO-MPC and the simulation settings are listed in Table II. Since the TO-MPC is synchronized with the SVM, current, torque, and flux ripples induced by the switching of the inverter are not visible in the following figures.

Based on torque step responses, the transient control performance of the proposed method is analyzed for different initial rotation angles $\varepsilon(t=0\,\mathrm{s})$ and different constant speeds. To illustrate the working principle of the TO-MPC an exemplary video animation is available in [30] for the same scenario as depicted in Fig. 3.

TABLE II
TO-MPC, PI-FOC, AND SIMULATIVE TEST SETUP PARAMETERS

Simulation setup		
Software	Simulink	
Solver	ode45 [29]	
Controller sampling period	T_s	62.5 µs
TO-MPC		
Number of RPR iterations	N	5
Dynamic current limit	$I_{max,dyn}$	270 A
D-axis current limit	$i_{d,max}$	20 A
PI-FOC		
Controller design	Magnitude optimum	
Dynamic overmodulation scheme	Minimum distance error [23]	
Anti-reset windup method	Back-calculation [31]	
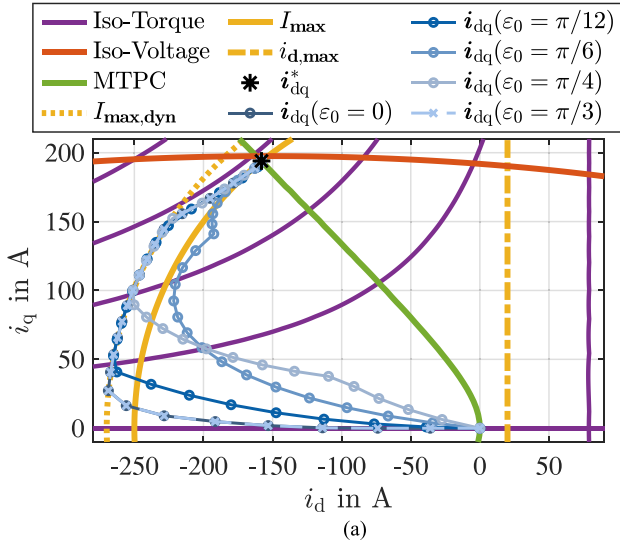
Fig. 6. Simulative TO-MPC trajectories for different initial rotor angles $\varepsilon(t=0\,\mathrm{s})=0$ at rated speed ($n_{me}=2750\,\mathrm{min}^{-1}$). (a) Current trajectories. (b) Flux linkage trajectories. (c) Torque trajectories.

A. Initial Rotor Angle Investigation

Due to the voltage constraint (32d) and the cost function (32a) of the TO-MPC, the corners (elementary vectors) of the voltage hexagon are preferred as input variables $\boldsymbol{u}_{\alpha\beta}$ during transients, since these often reduce the cost function the most as long as torque and current constraints (32c) are not active. For this reason, not only the flux linkage trajectory in the $\alpha\beta$-coordinate system during transients depends on the initial rotor angle, but also the current trajectories in the dq-coordinate system and the torque, see Fig. 6. Nevertheless, similar settling times for the torque without over- and undershootings of the torque and without violating the dynamic current limit $I_{max,dyn}$
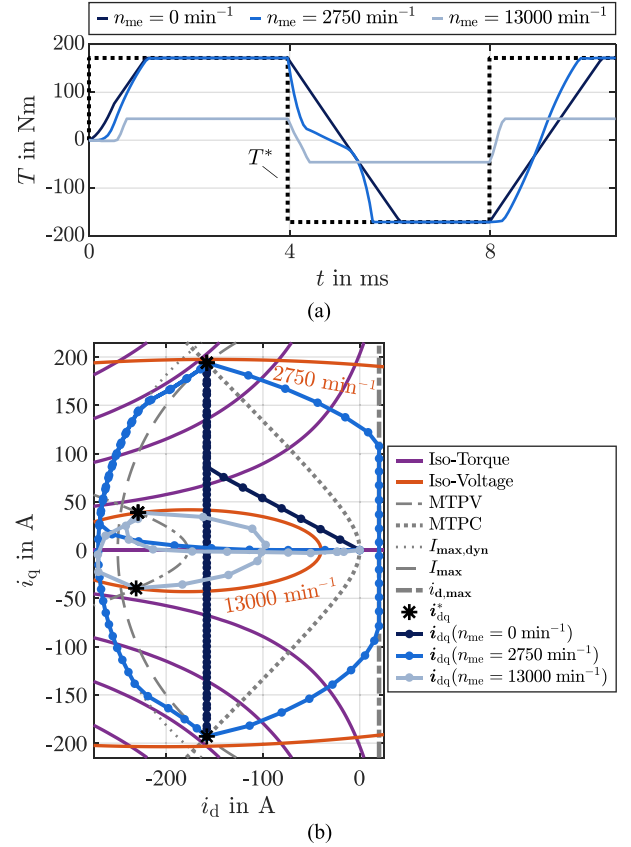

Fig. 7. Simulative TO-MPC trajectories for maximum and minimum torque operation for different speeds n_{me} with an initial rotor angle $\varepsilon(t=0\,\mathrm{s})=0$. (a) Torque trajectories. (b) Current trajectories.

are achieved, see Fig. 6(a) and (c). In Fig. 6(b), the flux linkage trajectories for a step response to the rated torque are depicted for equidistant distributed initial rotor angles $\varepsilon_0=\varepsilon(t=0\,\mathrm{s})$ from 0 to $\pi/3$. Here, the flux linkage trajectory for $\varepsilon_0=0$ is equal to the trajectory for $\varepsilon_0=\pi/3$ rotated by an angle of $-\pi/3$ due to the symmetry of the voltage hexagon and, therefore, results in identical dq current and torque trajectories.

B. Speed Dependency Investigation

Since the prerotation of the flux linkage reference depends on the angular velocity ω, the transient trajectories of torque and dq current differ during transient operation for different motor speeds n_{me} even for an identical initial rotor angle ε_0 and identical torque reference trajectories, see Fig. 7. Here, step responses to maximum and minimum torque are commanded. For speeds of $n_{me}=\{0, 2750\}\,\mathrm{min}^{-1}$ the maximum and minimum motor torque can be realized. However, for a speed of $n_{me}=13000\,\mathrm{min}^{-1}$, the OPC selects the intersections of the voltage limit and the MTPV trajectory as operating points $\boldsymbol{i}_{dq}^*$ which results in reduced torque magnitudes (flux weakening operation) compared to the rated operating point, cf., Fig. 7(b). Nevertheless, maximum and minimum possible torques are achieved.

Although the initial dq current $\boldsymbol{i}_{dq}(t=0\,\mathrm{s})=\boldsymbol{0}$ A is outside the voltage limit for $n_{me}=13000\,\mathrm{min}^{-1}$ and, thus, a torque undershoot is inevitable, the optimization problem (32) of the

TABLE III
REQUIRED SAMPLING INSTANTS TO CONDUCT THE OPERATING POINT
CHANGES DEFINED IN FIG. 3 FOR TOC WITH AND WITHOUT STATE
CONSTRAINTS AS WELL AS THE TO-MPC FOR $T_\mathrm{s} = 62.5\,\mu\mathrm{s}$, $\varepsilon(t=0\,\mathrm{s}) = 0$,
$n_\mathrm{me} = 2750\,\mathrm{min}^{-1}$, $I_\mathrm{max,dyn} = 270\,\mathrm{A}$, $i_\mathrm{d,max} = 20\,\mathrm{A}$

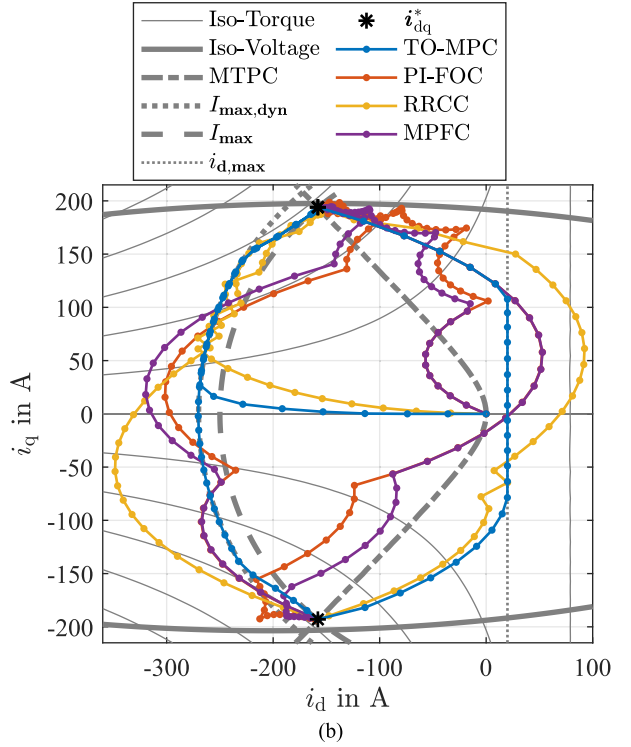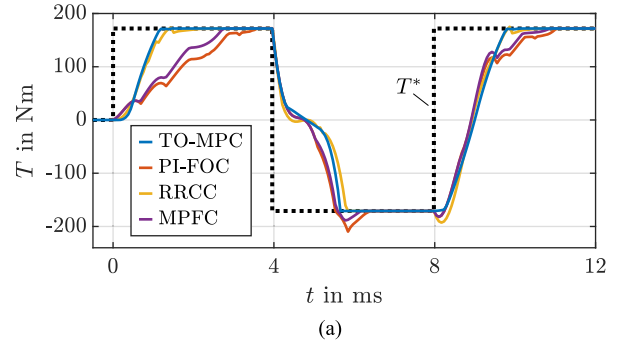| Operating point change	①	②	③	④	⑤	⑥
TOC w/o state constraints	23	26	22	14	28	14
TOC w/ state constraints	23	30	22	14	33	14
TO-MPC	23	30	22	14	33	14

Fig. 8. Simulative trajectories at rated speed ($n_\mathrm{me} = 2750\,\mathrm{min}^{-1}$) with an initial rotor angle $\varepsilon(t=0\,\mathrm{s}) = 0$. (a) Torque trajectories. (b) Current trajectories.

TO-MPC remains feasible due to its softened state constraints (32c) and a solution is found that limits the torque undershoot.

C. Time-Optimality Investigation

As a result of the state constraints (32c) the space of possible state trajectories during transient operation is restricted. To empirically investigate whether the TO-MPC leads to time-optimal trajectories even with active state constraints, the TO-MPC's control performance is compared to a TOC with the same torque and current constraints. This TOC with state constraints takes the whole future state and input trajectory during transient operation into account to minimize the time to reach the reference operating point i_dq^*, i.e., its prediction horizon is practically infinitely long. The resulting nonlinear constrained optimization problem was solved with a sequential quadratic programming algorithm of the MATLAB optimization toolbox. This is feasible for an offline simulation comparison, but of course the computational burden of the TOC solution is by far higher than the one step prediction required to solve the TO-MPC problem.

The sampling instants that are required to conduct the operating point changes of Fig. 3 for the TO-MPC and the TOC with state constraints are listed in Table III. Here, the TO-MPC achieves the same transient control performance as the TOC with state constraints. Thus, empirical evidence was provided that the TO-MPC solution requires the same transient performance as a TOC approach at significantly reduced computational cost (one-step versus unlimited prediction steps).

Furthermore, the required sampling instants for the TOC without state constraints are listed in Table III. This TOC corresponds to the deadbeat flux control law (21). It can be seen that only for the operating point changes ② and ⑤ the required sampling steps are reduced compared to the TOC with state constraints and the TO-MPC for the price of unintended transient current and torque trajectories, cf., Fig. 3.

D. Comparison to State-of-the-art Methods

In this section the control performance of the TO-MPC is compared to the state-of-the-art continuous-control-set methods of PI-FOC, RRCC [6], and a CCS-MPFC without state constraints and without RPR. Thus, the optimization problem of this simple, standard CCS-MPFC evaluates to

$$\min_{\boldsymbol{u}_{\alpha\beta}[k]} \|\hat{\boldsymbol{\psi}}_{\alpha\beta}[k+1] - \underbrace{\boldsymbol{T}_{\alpha\beta\mathrm{dq}}\left(\varepsilon[k] + T_\mathrm{s}\omega[k]\right)\boldsymbol{\psi}_\mathrm{dq}\left(\boldsymbol{i}_\mathrm{dq}^*[k]\right)}_{\boldsymbol{\psi}_{\alpha\beta}^*[k+1]}\|^2 \quad (33a)$$

$$\text{s.t.} \ \hat{\boldsymbol{\psi}}_{\alpha\beta}[k+1] = \boldsymbol{A}_\psi\hat{\boldsymbol{\psi}}_{\alpha\beta}[k] + \boldsymbol{B}_\psi\boldsymbol{u}_{\alpha\beta}[k] + \boldsymbol{E}_\psi[k] \quad (33b)$$

$$\boldsymbol{u}_{\alpha\beta}[k] \in \mathbb{U}_{\alpha\beta}. \quad (33c)$$

The parameters of the decoupled PI-FOC current controllers are listed in Table II. Compared to the PI-FOC, both the RRCC and CCS-MPFC (33) does not contain any tuning parameters. All controllers are sampled with $T_\mathrm{s} = 62.5\,\mu\mathrm{s}$ and synchronized with the SVM in the same way as the TO-MPC.

For this comparison, the same reference torque trajectory, as in Fig. 7(a) consisting of steps to rated motor and generator operation at rated speed ($n_\mathrm{me} = 2750\,\mathrm{min}^{-1}$) with an initial rotor angle $\varepsilon(t=0\,\mathrm{s}) = 0$ is selected. The resulting torque and current trajectories for the TO-MPC, PI-FOC, RRCC, and CCS-MPFC are depicted in Fig. 8. Since the torque and current constraints are not taken into account by the PI-FOC and CCS-MPFC, overcurrents and torque over- and undershoots
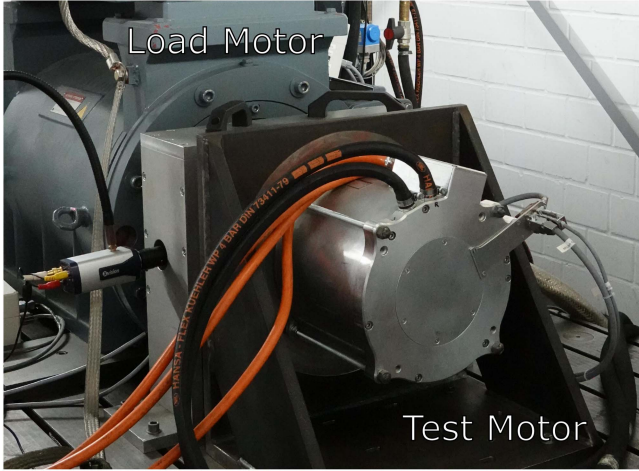
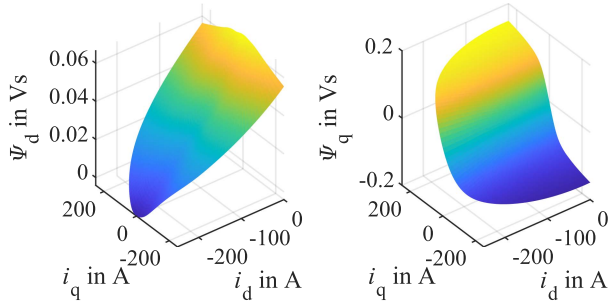Fig. 9. Test bench with load motor and test PMSM.

Fig. 10. Flux linkage maps of the utilized PMSM motor model.

cannot be prevented. Furthermore, increased settling times of the PI-FOC and CCS-MPFC especially for the transients starting at $t = 0$ ms and $t = 8$ ms can be observed compared to the TO-MPC and RRCC. The RRCC and the TO-MPC achieve similarly fast settling times since both use a prerotation of the reference flux linkage. However, the RRCC takes current and torque constraints only into account heuristically and, therefore, prevention of overcurrents and torque over- and undershoots cannot be guaranteed.

VII. EXPERIMENTAL INVESTIGATION

All following experimental results have been obtained on a laboratory test bench, see Fig. 9. The electrical drive system under test is a highly utilized interior permanent magnet synchronous motor (Brusa: HSM1-6.17.12-C01) for automotive applications and a two-level IGBT inverter (Semikron: 3×SKiiP 1242GB120-4D). The datasheet parameters, flux linkages and differential inductances can be seen in Table IV, Figs. 10 and 11. As load motor, a speed-controlled induction machine (Schorch: LU8250M-AZ83Z-Z) is mechanically coupled with the test motor. The test bench is further equipped with a dSPACE DS1006MC rapid-control-prototyping system. All measurements have been obtained by the dSPACE analog-digital-converters, which have been synchronized with the control task. The most important inverter, test bench, and control parameters are listed in Table IV.

TABLE IV
PMSM, DC-LINK, INVERTER, CONTROL, AND TEST BENCH PARAMETERS OF THE EXPERIMENTAL TEST SETUP

PMSM		Brusa HSM16.17.12-C01
Nominal power ($m = 0.907$)	P_{mech}	68 kW
Nominal speed ($m = 0.907$)	n_{mech}	4750 min^{-1}
Maximum speed	$n_{\text{mech,max}}$	11 000 min^{-1}
Nominal torque	T_{nom}	136 Nm
Pole pair number	p	3
DC-link voltage	u_{DC}	360 V
Nominal current	I	177 A
Stator resistance	R_{s}	18 mΩ
Permanent magnet flux	ψ_{p}	68 mVs
DC-link		Gustav Klein
Topology		DC-converter
DC-link capacitance		29 mF
Rated power		200 kW
Inverter		3×SKiiP 1242GB120-4D
Topology		Voltage-source inverter
		2-level, IGBT
Inverter interlocking time	T_{i}	3.3 μs
Switching frequency	f_{s}	8 kHz
TO-MPC		
Number of RPR iterations	N	5
Dynamic current limit	$I_{\text{max,dyn}}$	270 A
D-axis current limit	$i_{\text{d,max}}$	30 A
Gopinath-style flux observer		
Damping ratio	ξ	1
Crossover frequency	ω_0	1492 s^{-1}
Controller hardware		dSPACE
Processor board		DS1006MC, 4 cores, 2.8 GHz
Sampling time	T_{s}	62.5 μs
Measurement devices		
Oscilloscope		Tektronix MSO58
Current probes (zero-flux transducers)		3×Yokogawa, 500 A, 2 MHz
Torque sensor		HBM, T10FS, 2 kN m

TABLE V
TURNAROUND TIMES OF THE CONTROL STRATEGY

	Turnaround time in μs
OPC	8.4
GFO	2.3
RPR	0.9
CCS-MPFC	1.2-10.5
Auxiliary functions	30.6
Overall control strategy	43.4-52.7

The turnaround times of the OPC, GFO, RPR, CCS-MPFC, auxiliary functions and the overall control strategy are listed in Table V. Here, the low computational load of the RPR with an iteration number of $N = 5$ can be seen. The turnaround time reported for the auxiliary functions cover, e.g., SVM, coordinate transformations, analog-digital conversion, as well as processor and host computer communication that must be executed in addition to the OPC, GFO, RPR, and CCS-MPFC, are summarized. Compared to the other parts of the overall control scheme, the CCS-MPFC demands a variable number of calculation steps per controller sample. This is due to the varying required number of iteration steps for the utilized embedded active-set solver, cf., [26], [27], to find the global optimum of the QP (32). To reduce the number of iterations of the active-set solver the solution of the previous sampling instant was used as initial solution guess (hot start). Furthermore, in simulations and experiments it has not been observed that more than 11 iterations are required to find the optimum. Therefore, the required turnaround time of
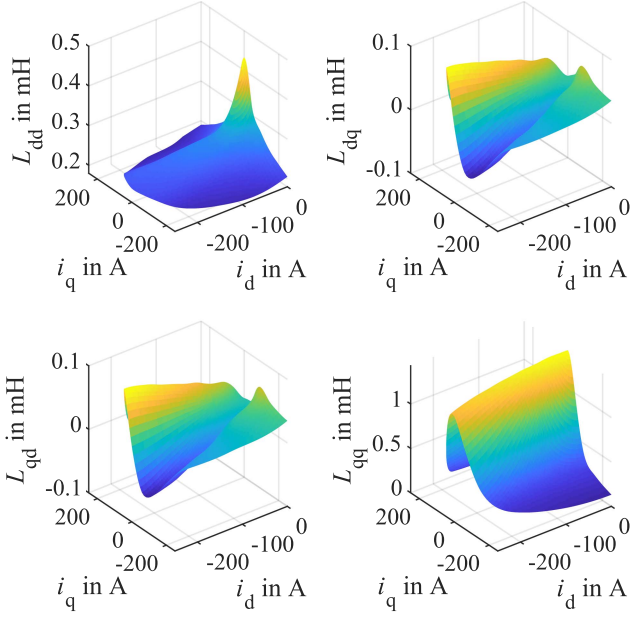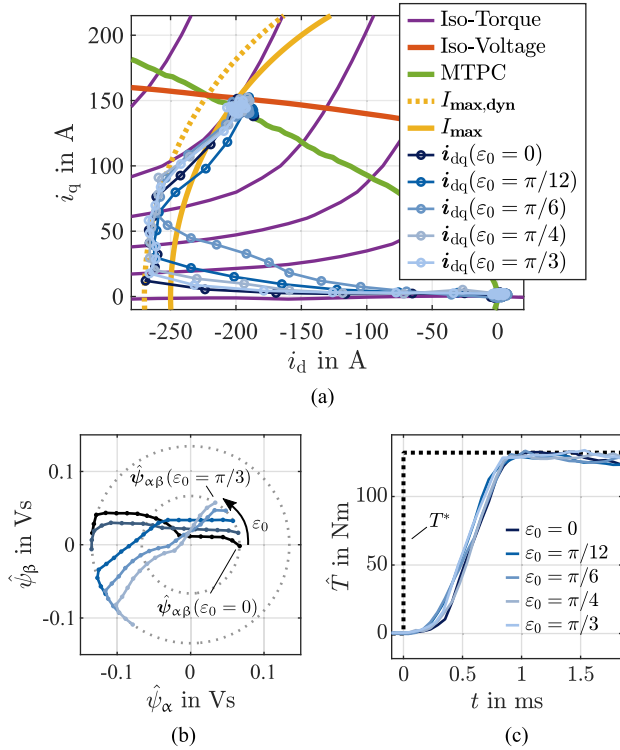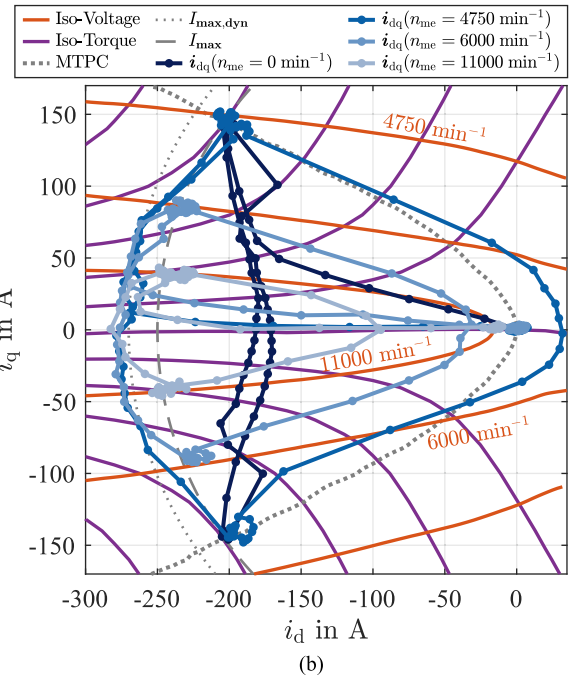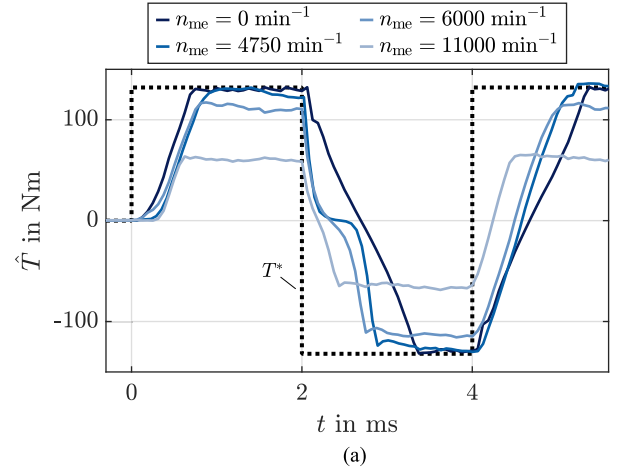
Fig. 11. Differential inductances maps of the utilized PMSM motor model.

Fig. 12. Experimental TO-MPC step response trajectories to maximum torque for different initial rotor angle $\varepsilon(t = 0\,\mathrm{s})$ at rated speed ($n_{\mathrm{me}} = 4750\,\mathrm{min}^{-1}$). (a) Current trajectories. (b) Flux linkage trajectories. (c) Torque trajectories.

Fig. 13. Experimental TO-MPC trajectories for maximum and minimum torque operation for different speeds n_{me} with an initial rotor angle $\varepsilon(t = 0\,\mathrm{s}) = 0$. (a) Torque trajectories. (b) Current trajectories.

1.2–10.5 µs corresponds to 1–11 iterations and leads to a varying turnaround time of the overall control strategy of 43.4–52.7 µs, see Table V.

In order to prove the effectiveness and performance of the TO-MPC, several representative experiments in the torque and speed range were carried out and are shown in the following. Since the discrete-time measurement samples are synchronized with the SVM, the current ripple induced by the switching of the inverter is not visible in the following figures. Furthermore, the torque, depicted in the following figures is not measured directly with the help of a torque sensor since highly dynamical experiments are investigated and, therefore, the moment of inertia of the rotor shaft as well as the limited bandwidth of the torque sensor distort the measurement. Instead, the torque is estimated via

$$\hat{T}[k] = \frac{3}{2}p\left(\hat{\psi}_\alpha[k]i_\beta[k] - \hat{\psi}_\beta[k]i_\alpha[k]\right). \tag{34}$$

A. Initial Angle Investigation

In Fig. 12, the trajectories for a step response to the rated torque are depicted for equidistant distributed initial rotor angles
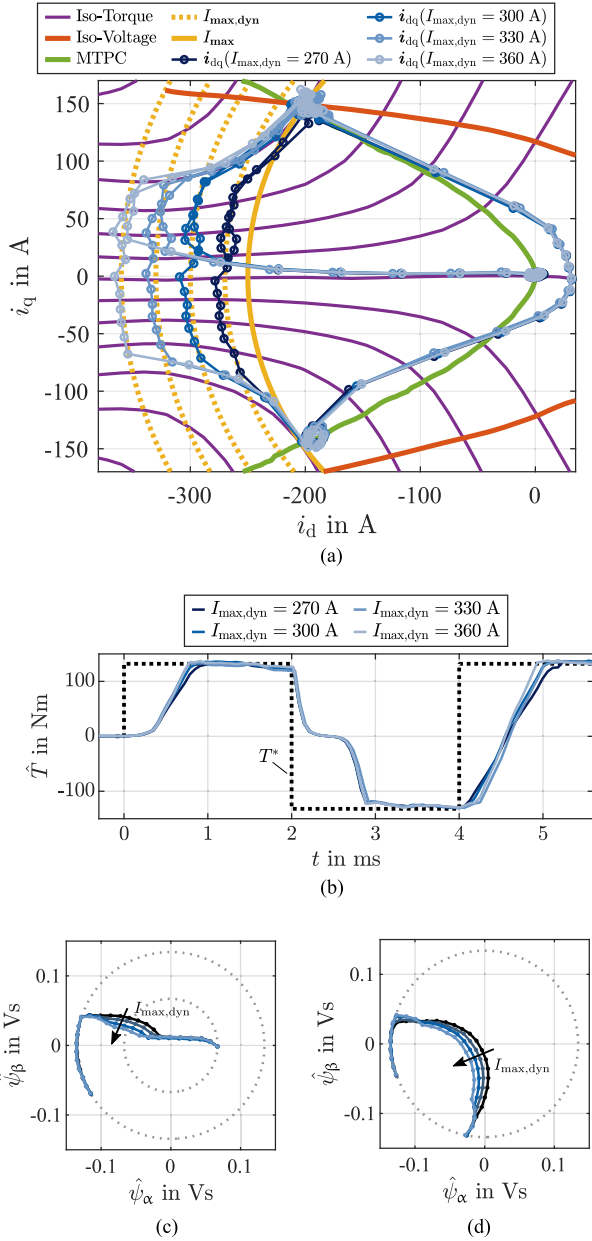
Fig. 14. Experimental TO-MPC step response trajectories to maximum torque for different dynamic current limits $I_{\mathrm{max,dyn}}$ at rated speed $(n_{\mathrm{me}} = 4750 \, \mathrm{min}^{-1})$ with an initial rotor angle $\varepsilon(t = 0 \, \mathrm{s}) = 0$. (a) Current trajectories. (b) Torque trajectories. (c) Flux linkage trajectories for the transient from t = 0 ms to t = 1.5 ms. (d) Flux linkage trajectories for the transient from t = 4 ms to t = 5.5 ms.

$\varepsilon_0 = \varepsilon(t = 0 \, \mathrm{s})$ from 0 to $\pi/3$ at rated speed. Here, torque over- and undershoots as well as overcurrents are prevented. Due to nonideal effects, e.g., parameter and model inaccuracies as well as measurement noise, prediction errors can lead to slight violations of the torque and current constraints. Nevertheless, these violations can be considered minor. Similar to the simulative investigation in Section VI-A for the linear-magnetized PMSM, the current trajectories differ for different initial rotor angles for the highly utilized PMSM with significant cross saturation, cf.,

Fig. 12(a). However, the resulting torque trajectories are similar for different initial rotor angles, see Fig. 12(c).

B. Speed Dependency Investigation

The torque and current trajectories for torque reference steps to rated motor and generator operation for different speeds in the whole speed range from standstill to maximum speed are depicted in Fig. 13. Due to the voltage limit for $n_{\mathrm{me}} = \{6000, 11000\} \, \mathrm{min}^{-1}$, the rated torque can no longer be achieved, see Fig. 13(a). However, the OPC ensures that the maximum and minimum possible torques are achieved for the corresponding speed. Because of the nonlinear magnetization, no sectionwise linear current trajectories occur at standstill compared to the current trajectories of the PMSM with linear magnetization, cf., Fig. 7(b).

C. Dynamic Current Limit Investigation

The state constraints (32c) ensure that any selected voltages $\boldsymbol{u}_{\alpha\beta}$ respect the dynamic current limit $I_{\mathrm{max,dyn}}$. Therefore, the dynamic current limit $I_{\mathrm{max,dyn}}$ restricts the set of feasible voltages $\boldsymbol{u}_{\alpha\beta}$ during transient operation at the current limit the more, the smaller $I_{\mathrm{max,dyn}}$ is chosen. To investigate the influence of the dynamic current limit, the torque, current, and flux linkage trajectories are depicted in Fig. 14 for torque reference steps to rated motor and generator operation at rated speed $n_{\mathrm{me}} = 4750 \, \mathrm{min}^{-1}$. Here, slightly reduced settling times of the torque for increased dynamic current limits $I_{\mathrm{max,dyn}}$ can be observed since the trajectories of the currents reach the isotorque loci earlier, see Fig. 14(a). However, the flux linkage reference operating points are reached with similar settling times, cf., Fig. 14(c) and (d). During the transient from the rated generator to motor operating point at approx. 4 ms, there are current samples near the d-axis which are slightly below and above the dynamic current limit $I_{\mathrm{max,dyn}}$. This deviation of the current trajectory from the dynamic current limit can be explained by prediction errors of the current prediction model (11) due to the rapidly varying differential inductance L_{qq}, cf., Fig. 11.

VIII. CONCLUSION AND OUTLOOK

In this article, the concept of TO-MPC for PMSM was proposed and investigated in the whole speed and torque range via simulations and experiments. Here, TOC performance is achieved with the help of a prerotation of the flux linkage reference for a CCS-MPFC. Thanks to the incorporation of linearized time-varying current and torque limits as softened state constraints of the TO-MPC, overcurrents as well as torque over- and undershoots can be effectively prevented compared to the state-of-the-art TOC methods for PMSMs.

In the future, the extension of the TO-MPC to the overmodulation range up to the six-step operation will be investigated. This should be achieved by incorporating the harmonic reference generator approach presented in [32] with the prerotation of the flux linkage reference to enable TO-MPC in the whole modulation range.

REFERENCES

[1] M. Spichartz, M. Oettmeier, C. Heising, V. Staudt, and A. Steimel, "Stator-flux-oriented control with high torque dynamics for IM and PMSM," in *Proc. IEEE Veh. Power Propulsion Conf.*, 2010, pp. 1–6.

[2] C. Jong-Woo and S. Sul, "Generalized solution of minimum time current control in three-phase balanced systems," *IEEE Trans. Ind. Electron.*, vol. 45, no. 5, pp. 738–744, Oct. 1998.

[3] S. Bolognani, M. Tomasini, L. Tubiana, and M. Zigliotto, "DSP-based time optimal current control for high dynamic IPM motor drives," in *Proc. IEEE 35th Annu. Power Elec. Specialists Conf.*, 2004, vol. 3, pp. 2197–2203.

[4] Y. Wang et al., "Fast response model predictive torque and flux control with low calculation effort for PMSMs," *IEEE Trans. Ind. Informat.*, vol. 15, no. 10, pp. 5531–5540, Oct. 2019.

[5] H. Khatib, D. Gerling, and M. Saur, "Deadbeat flux vector control as a one single control law operating in the linear, overmodulation, and six-step regions with time-optimal torque control," *IEEE Open J. Ind. Appl.*, vol. 3, pp. 247–270, 2022.

[6] W. Wang, M. Du, and K. Wei, "Rapid torque rising of PMSM by directly chasing rotating flux linkage vector," *IEEE J. Emerg. Sel. Topics Power Electron.*, vol. 9, no. 4, pp. 4384–4394, Aug. 2021.

[7] W. Peters, O. Wallscheid, and J. Böcker, "A precise open-loop torque control for an interior permanent magnet synchronous motor considering iron losses," in *Proc. 38th Annu. Conf. IEEE Ind. Electron. Soc.*, 2012, pp. 2877–2882.

[8] J. S. Lee, C. Choi, J. Seok, and R. D. Lorenz, "Deadbeat-direct torque and flux control of interior permanent magnet synchronous machines with discrete time stator current and stator flux linkage observer," *IEEE Trans. Ind. Appl.*, vol. 47, no. 4, pp. 1749–1758, Jul./Aug. 2011.

[9] L. Zhong, M. F. Rahman, W. Y. Hu, and K. W. Lim, "Analysis of direct torque control in permanent magnet synchronous motor drives," *IEEE Trans. Power Electron.*, vol. 12, no. 3, pp. 528–536, May 1997.

[10] M. Preindl, "Robust control invariant sets and Lyapunov-based MPC for IPM synchronous motor drives," *IEEE Trans. Ind. Electron.*, vol. 63, no. 6, pp. 3925–3933, Jun. 2016.

[11] A. Favato, P. G. Carlet, F. Toso, R. Torchio, and S. Bolognani, "Integral model predictive current control for synchronous motor drives," *IEEE Trans. Power Electron.*, vol. 36, no. 11, pp. 13293–13303, Nov. 2021.

[12] S. Wendel, P. Karamanakos, P. Gebhardt, A. Dietz, and R. Kennel, "Flux linkage-based direct model predictive current control for synchronous machines," *IEEE Trans. Power Electron.*, vol. 36, no. 12, pp. 14237–14256, Dec. 2021.

[13] S. Hanke, O. Wallscheid, and J. Böcker, "Continuous-control-set model predictive control with integrated modulator in permanent magnet synchronous motor applications," in *Proc. IEEE Int. Elect. Mach. Drives Conf.*, 2019, pp. 2210–2216.

[14] C. M. Hackl, J. Kullick, H. Eldeeb, and L. Horlbeck, "Analytical computation of the optimal reference currents for MTPC/MTPA, MTPV and MTPF operation of anisotropic synchronous machines considering stator resistance and mutual inductance," in *Proc. 19th Eur. Conf. Power Electron. Appl.*, 2017, pp. P.1–P.10.

[15] H. Eldeeb, C. M. Hackl, L. Horlbeck, and J. Kullick, "A unified theory for optimal feedforward torque control of anisotropic synchronous machines," *Int. J. Control*, vol. 91, no. 10, pp. 2273–2302, 2018.

[16] P. L. Jansen and R. D. Lorenz, "A physically insightful approach to the design and accuracy assessment of flux observers for field oriented induction machine drives," *IEEE Trans. Ind. Appl.*, vol. 30, no. 1, pp. 101–110, Jan./Feb. 1994.

[17] A. Yoo and S. Sul, "Design of flux observer robust to parameter variation of interior permanent magnet synchronous motor," in *Proc. IEEE Ind. Appl. Soc. Annu. Meeting*, 2008, pp. 1–7.

[18] H. W. van der Broeck, H. C. Skudelny, and G. V. Stanke, "Analysis and realization of a pulsewidth modulator based on voltage space vectors," *IEEE Trans. Ind. Appl.*, vol. 24, no. 1, pp. 142–150, Jan./Feb. 1988.

[19] A. Specht, S. Ober-Blöbaum, O. Wallscheid, C. Romaus, and J. Böcker, "Discrete-time model of an IPMSM based on variational integrators," in *Proc. IEEE Int. Elect. Mach. Drives Conf.*, 2013, pp. 1411–1417.

[20] J. Böcker, "Discrete-time model of an induction motor," *Eur. Trans. Elect. Power*, vol. 1, no. 2, pp. 65–71, 1991.

[21] W. Peters and J. Böcker, "Discrete-time design of adaptive current controller for interior permanent magnet synchronous motors (IPMSM) with high magnetic saturation," in *Proc. 39th Annu. Conf. IEEE Ind. Electron. Soc.*, 2013, pp. 6608–6613.

[22] A. Brosch, O. Wallscheid, and J. Böcker, "Model predictive control of permanent magnet synchronous motors in the overmodulation region including six-step operation," *IEEE Open J. Ind. Appl.*, vol. 2, pp. 47–63, 2021.

[23] F. Briz, A. Diez, M. W. Degner, and R. D. Lorenz, "Current and flux regulation in field-weakening operation of induction motors," *IEEE Trans. Ind. Appl.*, vol. 37, no. 1, pp. 42–50, Jan./Feb. 2001.

[24] E. Kerrigan and J. Maciejowski, "Soft constraints and exact penalty functions in model predictive control," in *Proc. Control Conf.*, 2000.

[25] M. Zeilinger, M. Morari, and C. Jones, "Soft constrained model predictive control with robust stability guarantees," *IEEE Trans. Autom. Control*, vol. 59, no. 5, pp. 1190–1202, May 2014.

[26] N. Khaled and B. Pattel, *Practical Design and Application of Model Predictive Control: MPC for MATLAB and Simulink Users*. London, U.K.: Butterworth-Heinemann, 2018.

[27] C. Schmid and L. Biegler, "Quadratic programming methods for reduced Hessian SQP," *Comput. Chem. Eng.*, vol. 18, no. 9, pp. 817–832, 1994.

[28] P. Cortes, J. Rodriguez, C. Silva, and A. Flores, "Delay compensation in model predictive current control of a three-phase inverter," *IEEE Trans. Ind. Electron.*, vol. 59, no. 2, pp. 1323–1325, Feb. 2012.

[29] N. Senan, "A brief introduction to using ode45 in MATLAB," Dept. of Mech. Eng., Univ. of California at Berkeley, Berkeley, CA, USA, 2007.

[30] A. Brosch, O. Wallscheid, and J. Böcker, "Animation of the to-MPC." [Online]. Available: https://doi.org/10.1109/TPEL.2023.3265705/mm1

[31] K. J. Åström and T. Hägglund, *Advanced PID control*. Pittsburgh, PA, USA: ISA - The Instrum. Syst. Automat. Soc., 2006.

[32] A. Brosch, O. Wallscheid, and J. Böcker, "Model predictive torque control for permanent magnet synchronous motors using a stator-fixed harmonic flux reference generator in the entire modulation range," *IEEE Trans. Power Electron.*, vol. 38, no. 4, pp. 4391–4404, Apr. 2023.

Anian Brosch received the bachelor's and master's degrees in mechanical engineering from the Munich University of Applied Sciences, Munich, Germany, in 2016 and 2018, respectively.

Since then, he has been a Research Associate with the Department of Power Electronics and Electrical Drives, Paderborn University, Paderborn, Germany. His research interests include identification and control of electrical drives, in particular model predictive control of highly utilized permanent magnet synchronous motors.

Oliver Wallscheid (Member, IEEE) received the bachelor's and master's degrees (honors) in industrial engineering and the doctorate degree (honors) in electrical engineering in 2010, 2012 and 2017, respectively, all from Paderborn University, Paderborn, Germany.

Since then, he has been a Senior Research Fellow with the Department of Power Electronics and Electrical Drives, Paderborn University. His research interests include data-driven identification and intelligent control of electrical power systems in decentralized grids, power electronics and drives.

Joachim Böcker (Senior Member, IEEE) received the diploma degree (German degree equivalent to international master in engineering) in electrical engineering and the Dr.-Ing. degree from the Berlin University of Technology, Berlin, Germany, in 1982 and 1988, respectively.

He is a Professor and Head with the Department of Power Electronics and Electrical Drives, Paderborn University, Paderborn, Germany. From 1988 to 2001, he was with AEG and Daimler Research as Head of the control engineering team of the Electrical Drive Systems Laboratory. In 2001, he started his own business in the area of control engineering, electrical drives, and power electronics. In 2003, he was appointed to the current professorship. His research interests include electrical drives, particularly for EVs and HEVs, energy management strategies for vehicles and smart grids, and converters for power supplies, EV chargers, and renewables.